SHM
Structural Health Monitoring

Damage Detection in Thin Plates and Aerospace Structures with the Electro-Mechanical Impedance Method

Victor Giurgiutiu[1,*] and Andrei Zagrai[2]

[1]*Mechanical Engineering Department, University of South Carolina Columbia, SC 29208, USA*
[2]*Davidson Laboratory, Stevens Institute of Technology, Castle Point on Hudson, Hoboken, NJ 07030, USA*

The use of the electro-mechanical (E/M) impedance method for health monitoring of thin plates and aerospace structures is described. As a nondestructive evaluation technology, the E/M impedance method allows us to identify the local dynamics of the structure directly through the E/M impedance signatures of piezoelectric wafer active sensors (PWAS) permanently mounted to the structure. An analytical model for 2-D thin-wall structures, which predicts the E/M impedance response at PWAS terminals, was developed and validated. The model accounts for axial and flexural vibrations of the structure and considers both the structural dynamics and the sensor dynamics. Calibration experiments performed on circular thin plates with centrally attached PWAS showed that the presence of damage modifies the high-frequency E/M impedance spectrum causing frequency shifts, peak splitting, and appearance of new harmonics. Overall-statistics damage metrics and probabilistic neural network (PNN) are used to classify the spectral data and identify damage severity. On thin-wall aircraft panels, the presence of damage influences the sensors E/M impedance spectrum. When crack damage is in the PWAS medium field, changes in the distribution of harmonics take place and when crack damage is in the PWAS near field, changes in both the harmonics and the dereverberated response are observed. These effects are successfully classified with PNN and overall-statistics metrics, respectively. This proves that permanently attached PWAS in conjunction with the E/M impedance method can be successfully used in structural health monitoring to detect the presence of incipient damage through the examination and classification of the high-frequency E/M impedance spectra.

Keywords electro-mechanical impedance · piezoelectric wafer active sensors · vibration of circular plates · aging aircraft · structural health monitoring · overall statistics · neural networks · E/M impedance · PWAS · EMI · SHM · IVHM · PNN

1 Introduction

Structural health monitoring (SHM) could play a considerable role in maintaining the safety of aging aerospace vehicles subjected to heavy fatigue loads. For such structures, the development of an integrated sensory system able to monitor, collect, and deliver the structural health information is

*Author to whom correspondence should be addressed.
E-mail: victorg@sc.edu

Vol 4(2): 0099–20
[1475-9217 (200506) 4:2;99–20; 10.1177/1475921705049752]

essential. The upfront cost associated with implementing the SHM systems may be considerable. This aspect is of concern to both the manufacturers and the operators. A full cost-benefit analysis is needed; such an analysis would have to be performed in cooperation with the manufacturers and the operators. It is envisaged that the life cycle cost of the complete fleet will noticeably decrease after the full implementation of SHM systems.

One of the proposed approaches is to utilize arrays of piezoelectric wafers attached to the surface of a metallic structure or inserted between the layers of a composite material. When attached to the structure and connected to the electronics, these piezoelectric wafers become active sensors that can act as both actuators and detectors of elastic waves in the structure. For lack of a better term, we have called them PWAS, which is short for piezoelectric wafer active sensors. PWAS are the enabling element in the E/M impedance method [2], which is able to assess the local structural response at very high frequencies (typically hundreds of kilohertz). This high-frequency response is not affected by the global structural modes and environmental conditions such as flight loads and ambient vibrations. Thus, the E/M impedance method allows monitoring of incipient local damage (i.e., cracks, disbonds, delamination, etc.), which produces only imperceptible and hardly noticeable changes to the large-scale dynamics of the entire structure. For this reason, the high-frequency E/M impedance method can detect localized small damage that is otherwise undetectable with conventional vibration methods.

The E/M impedance method has been tried for the SHM of various structural components and engineering structures. The local-area health monitoring of a tail-fuselage aircraft junction was described by Chaudhry et al. [1]. Giurgiutiu et al. [2] used the E/M impedance method to detect near-field damage in realistic built-up panels representative of aging aircraft structures. The implementation of E/M impedance method for detecting delamination and crack growth on composite-reinforced concrete walls was presented by Raju et al. [3]. More developments in the E/M impedance method were discussed by Giurgiutiu and Rogers [4] and by Park and Inman [5]. An extensive study of the damage metrics suitable for E/M impedance SHM was presented by Tseng et al. [6] who used an overall statistics approach to quantify the presence of damage, and found that the correlation coefficient gave best results. A comprehensive review of the impedance method was recently published by Park et al. [28].

Pioneering work on the analysis of sensor–structure interaction in E/M impedance method was presented by Liang et al. [7] and Sun et al. [8]. Further model development was attempted by Zhou et al. [9] and Esteban [10], but they did not derive explicit expressions for predicting the E/M impedance as it would be measured by the impedance analyzer at the terminals of a structurally attached PWAS. Park et al. [11] performed the axial vibrations analysis of a bar, but did not consider the flexural response, or the sensor dynamics. Giurgiutiu and Zagrai [12] derived an expression for the E/M admittance and impedance that incorporates both the sensor dynamics and the structural dynamics. In the structural dynamics, they included both the flexural and the axial modes. However, their analysis was limited to 1-D structures. The present paper continues this analytical effort and extends it to 2-D structures, specifically circular thin plates with centrally located PWAS.

2 Modeling of the Interaction between a PWAS and a Circular Plate

Assume a thin isotropic circular plate with a PWAS surface mounted at its center (Figure 1). Under PWAS excitation, both axial and flexural vibrations are set in motion. The structural dynamics affects the PWAS response, and modifies its electro-mechanical impedance, i.e., the impedance measured by an impedance analyzer connected to the PWAS terminals. The purpose of this section is to model the interaction between the PWAS and the structure, and predict the impedance spectrum that would be measured at the PWAS terminals during the structural identification process. In our development, we will account for both the structural dynamics and the PWAS dynamics. The interaction between the

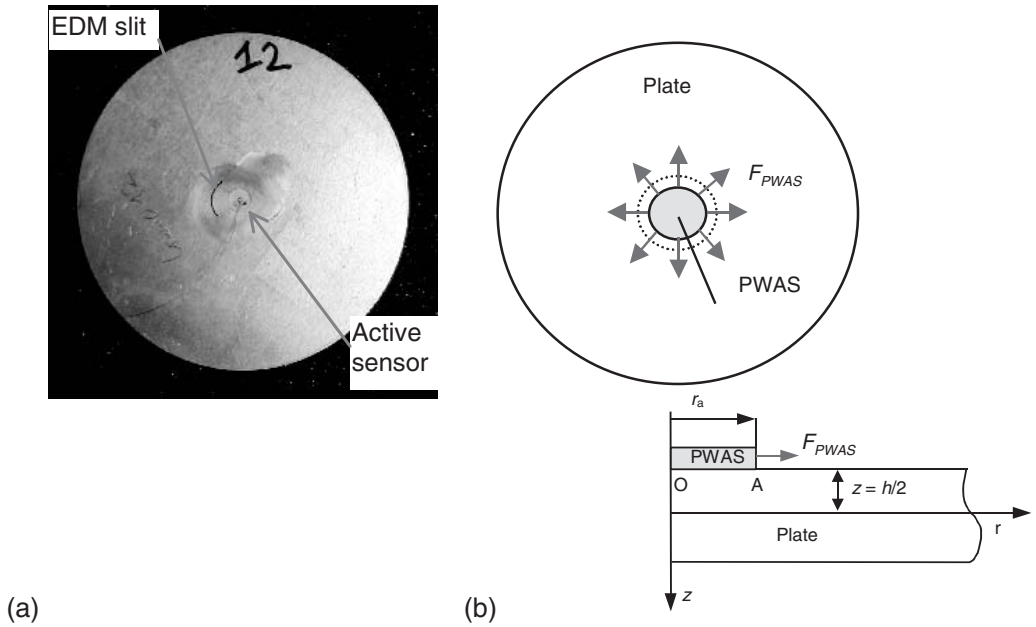

Figure 1 (a) PWAS mounted on a circular plate and (b) PWAS and plate schematics.

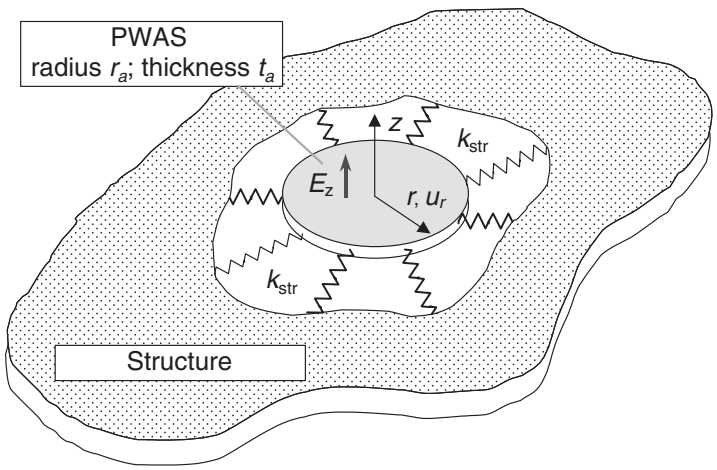

Figure 2 Piezoelectric wafer active sensor constrained by structural stiffness, $k_{str}(\omega)$.

PWAS, and the structure is modeled as shown in Figure 2. The structure is assumed to present to the PWAS, an effective structural dynamic stiffness, $k_{\text{str}}(\omega)$, which on the excitation frequency in strict correlation with the local structural dynamics, will include both axial and flexural modes. The problem is formulated in terms of interaction line force, F_{PWAS}, and the corresponding displacement, u_{PWAS}, measured at the PWAS circumference. The assumption implied in this model is that the surface adhesion between the PWAS and the structure can be reduced to an effective boundary interaction between the radial displacement and the line force at the PWAS circumference (similar to the pin–force model in 1-D analysis of PWAS–structure interaction).

When the PWAS is excited with an oscillatory voltage, its volume expands in phase with the voltage in accordance with the piezoelectric effect. Expansion of the PWAS mounted to the surface of the plate induces a surface reaction from the plate in the form of the line force

distributed around the PWAS circumference, $F_{\mathrm{PWAS}}(t) = \hat{F}_{\mathrm{PWAS}} e^{i\omega t}$. The reaction force, $F_{\mathrm{PWAS}}(t)$, depends on the PWAS radial displacement, $u_{\mathrm{PWAS}}(t)$, and on the frequency-dependent dynamic stiffness, $k_{\mathrm{str}}(\omega)$, presented by the structure to the PWAS:

$$F_{\mathrm{PWAS}}(t) = k_{\mathrm{str}}(\omega) \cdot u_{\mathrm{PWAS}}(t) \tag{1}$$

2.1 Modeling of the PWAS Electro-mechanical Impedance

To model the circular-shaped PWAS, we start from the piezoelectric constitutive equations in cylindrical coordinates as [13–15]:

$$\begin{aligned} S_{rr} &= s_{11}^E T_{rr} + s_{12}^E T_{\theta\theta} + d_{31} E_z \\ S_{\theta\theta} &= s_{12}^E T_{rr} + s_{11}^E T_{\theta\theta} + d_{31} E_z \\ D_z &= d_{31}(T_{rr} + T_{\theta\theta}) + \varepsilon_{33}^T E_z \end{aligned} \tag{2}$$

S_{rr} and $S_{\theta\theta}$ are the mechanical strains, T_{rr} and $T_{\theta\theta}$, the mechanical stresses, E_z the electrical field, D_z the electrical displacement, s_{11}^E and s_{12}^E the mechanical compliances at zero electric field ($E=0$), ε_{33}^T the dielectric permittivity at zero mechanical stress ($T=0$), and d_{31} the piezoelectric coupling between the electrical and mechanical variables. For axisymmetric motion, the problem is θ-independent and the space variation is in r only. Hence, $S_{rr} = \partial u_r/\partial r$ and $S_{\theta\theta} = u_r/r$. Applying Newton's second law, one recovers, upon substitution, the wave equation in polar coordinates:

$$\frac{\partial^2 u_r}{\partial r^2} + \frac{1}{r}\frac{\partial u_r}{\partial r} - \frac{u_r}{r^2} = \frac{1}{c^2}\frac{\partial^2 u_r}{\partial t^2} \tag{3}$$

where $c = 1/\sqrt{\rho s_{11}^E \cdot (1-\nu_a^2)}$ is the sound speed in the PWAS for axially symmetric radial motion, with ν_a the Poisson's ratio of the piezoelectric material ($\nu_a = -s_{12}^E/s_{11}^E$). Equation (3) admits a general solution in terms of Bessel functions of the first kind, J_1, in the form

$$u_r(r,t) = A \cdot J_1\left(\frac{\omega r}{c}\right) e^{i\omega t} \tag{4}$$

where, the coefficient A is determined from the normalization condition. When the PWAS is mounted on the structure, its circumference is elastically constrained by the dynamic structural stiffness (Figure 2). Although a solution for the case of a free boundary condition at the circumference exists in the literature [14], no solution has been found for the case when the circumferential boundary condition is in the form of an elastic constraint of known dynamic stiffness, $k_{\mathrm{str}}(\omega)$. Hence, we develop this solution here. At the boundary $r = r_a$,

$$T_{rr}(r_a) \cdot t_a = k_{str}(\omega) \cdot u_r(r_a) \tag{5}$$

where t_a is the PWAS thickness. Hence, the radial stress can be expressed as:

$$T_{rr}(r_a) = \frac{k_{str}(\omega) \cdot u_r(r_a)}{t_a} \tag{6}$$

Substitution of Equation (6) into Equation (2) gives, upon rearrangement,

$$\begin{aligned} \frac{\partial u_r(r_a)}{\partial r} = \chi(\omega) \cdot (1+\nu_a)\frac{u_r(r_a)}{r_a} - \nu_a \frac{u_r(r_a)}{r_a} \\ + (1+\nu_a) d_{31} E_z \end{aligned} \tag{7}$$

where, $\chi(\omega) = k_{\mathrm{str}}(\omega)/k_{\mathrm{PWAS}}$ is the dynamic stiffness ratio, and $k_{\mathrm{PWAS}} = t_a/r_a s_{11}^E(1-\nu_a)$ is the static stiffness of the piezoelectric disk. Substitution of Equation (4) into Equation (7) yields:

$$\begin{aligned} A = ((1+\nu_a) \cdot d_{31} E_0) \Big/ \big((\omega/c) J_0(\omega r_a/c) \\ - (1 - \nu_a + \chi(\omega) \cdot (1+\nu_a))/r_a \cdot J_1(\omega r_a/c) \big) \end{aligned} \tag{8}$$

The electrical admittance is calculated as the ratio between the current and the voltage amplitudes, i.e., $Y = \hat{I}/\hat{V}$. The current is calculated by integrating the electric displacement D_z over the PWAS area to obtain the total charge, and then differentiating with respect to time, while the voltage is calculated by multiplying the electric field by the PWAS thickness. Hence, the electrical admittance is expressed as:

$$Y(\omega) = i\omega C\left(1 - k_p^2\right) \cdot \left[1 + \frac{k_p^2}{1-k_p^2} \frac{(1+\nu_a) J_1(\varphi_a)}{\varphi_a J_0(\varphi_a) - (1-\nu_a) J_1(\varphi_a) - \chi(\omega)(1+\nu_a) J_1(\varphi_a)} \right] \tag{9}$$

where, $\varphi_a = \omega r_a/c$ and $k_p = \sqrt{2d_{31}^2/[s_{11}^E \cdot (1-\nu_a)\varepsilon_{33}^T]}$ is the planar coupling factor. Then, the inverse relationship between impedance and admittance, $Z(\omega) = 1/Y(\omega)$, yields:

$$Z(\omega) = \left\{ i\omega C\left(1-k_p^2\right) \cdot \left[1 + \frac{k_p^2}{1-k_p^2} \frac{(1+\nu_a)J_1(\varphi_a)}{\varphi_a J_0(\varphi_a) - (1-\nu_a)J_1(\varphi_a) - \chi(\omega)(1+\nu_a)J_1(\varphi_a)} \right] \right\}^{-1} \tag{10}$$

Equation (10) predicts the E/M impedance spectrum, as it would be measured by the impedance analyzer at the embedded PWAS terminals during a SHM process, and it allows for direct comparison between calculated predictions and experimental results. The structural dynamic is reflected in Equation (10) through the dynamic stiffness factor, $\chi(\omega) = k_{\text{str}}(\omega)/k_{\text{PWAS}}$, which contains the dynamic stiffness of the structure, $k_{\text{str}}(\omega)$. This latter quantity results from the analysis of the circular plate dynamics, as described here.

2.2 Modeling of the Circular Plate Dynamics

The equations for axisymmetric axial and flexural vibrations of circular plates are assumed in the form [16–18]:

$$\frac{Eh}{1-\nu^2}\left(\frac{\partial^2 u}{\partial r^2} + \frac{1}{r}\frac{\partial u}{\partial r} - \frac{u}{r^2}\right) - \rho h \cdot \frac{\partial^2 u}{\partial t^2} = -\left(\frac{\partial N_r^e}{\partial r} + \frac{N_r^e}{r}\right) \tag{11}$$

$$D\nabla^4 w + \rho h \cdot \frac{\partial^2 w}{\partial t^2} = \frac{\partial^2 M_r^e}{\partial r^2} + \frac{2}{r}\frac{\partial M_r^e}{\partial r} \tag{12}$$

where u is the in-plane displacement along the r-direction, w is the transverse displacement, h is the plate thickness, and ρ is the plate density. The quantities N_r^e and M_r^e are excitation line forces and line moments acting over the whole surface of the plate. These excitation forces and moments originate in the PWAS force, $F_{\text{PWAS}}(t)$, acting at the surface of the plate at $r = r_a$. Resolving this force at the plate midplane, we get a line force and a line moment acting:

$$\begin{aligned} N_a(t) &= F_{\text{PWAS}}(t) \\ M_a(t) &= \frac{h}{2} F_{\text{PWAS}}(t) \end{aligned} \tag{13}$$

Using the Heaviside step function, we write:

$$\begin{aligned} N_r^e(r,t) &= N_a(t) \cdot [-H(r_a - r)] \\ M_r^e(r,t) &= M_a(t) \cdot [H(r_a - r)], \qquad r \in [0,\infty) \end{aligned} \tag{14}$$

The steady state solution of Equations (11) and (12) are sought as modal expansions:

$$\begin{aligned} u(r,t) &= \left(\sum_k P_k R_k(r)\right) \cdot e^{i\omega t} \\ w(r,t) &= \left(\sum_m G_m \cdot Y_m(r)\right) \cdot e^{i\omega t} \end{aligned} \tag{15}$$

where P_k and G_m are the modal participation factors for axial and flexural vibrations, while $R_k(r)$ and $Y_m(r)$ are the corresponding mode shapes. For free-edge boundary conditions, the axisymmetric mode shapes $R_k(r)$ and $Y_m(r)$ are expressed in terms of Bessel functions [19]:

$$\begin{aligned} R_k(r) &= A_k J_1(\lambda_k r) \\ Y_m(r) &= A_m \cdot [J_0(\lambda_m r) + C_m \cdot I_0(\lambda_m r)] \end{aligned} \tag{16}$$

The mode shapes $R_k(r)$ and $Y_m(r)$ form orthonormal function sets that satisfy the orthonormality conditions:

$$\begin{aligned} \rho h \cdot \int_0^a \int_0^{2\pi} R_k(r) R_l(r) r dr d\theta &= \rho h \cdot \pi a^2 \cdot \delta_{kl} \\ \rho h \cdot \int_0^a \int_0^{2\pi} Y_p(r) \cdot Y_m(r) r dr d\theta &= m \cdot \delta_{pm} \\ &= \pi a^2 \cdot \rho h \cdot \delta_{pm} \end{aligned} \tag{17}$$

where, a is the outer radius of the circular plate and δ_{ij} are the Kroneker's deltas. Equations

(13)–(17), yield the modal participation factors for axial and flexural vibrations:

$$P_k = \frac{2N_a}{\rho h \cdot a^2} \cdot \frac{\left[r_a R_k(r_a) - \int_0^a R_k(r) H(r_a - r) dr\right]}{\left(\omega_k^2 - 2i\varsigma_k \omega\omega_k + \omega^2\right)}$$

$$G_m = \frac{2M_a}{\rho h \cdot a^2} \frac{\left[3Y_m(r_a) + r_a \cdot Y_m^{/}(r_a)\right]}{\left(\omega_m^2 - 2i\varsigma_m \omega\omega_m + \omega^2\right)} \tag{18}$$

where ζ_k and ζ_m are modal damping ratios. The detailed derivation of modal participation factors can be found in [20].

2.3 Calculation of the Effective Structural Stiffness

We calculate the effective structural stiffness $k_{\text{str}}(\omega)$ from the structural response to PWAS excitation. The radial displacement at the rim of the PWAS can be expressed in the form:

$$u_{\text{PWAS}}(r_a,t) = u(r_a,t) - \frac{h}{2} \cdot w^{/}(r_a,t) \tag{19}$$

Note that $u(r_a,t)$ and $w(r_a,t)$ represent displacements at the plate midsurface, while $u_{\text{PWAS}}(r_a,t)$ is measured at the plate upper surface (Figure 1). Using Equation (15), we write

$$u_{\text{PWAS}}(r_a,t) = \sum_k P_k R_k(r_a) \cdot e^{i\omega t} - \frac{h}{2} \sum_m G_m Y_m^{/}(r_a) \cdot e^{i\omega t} \tag{20}$$

Substitution of Equations (18) into Equation (20) yields the PWAS displacement in terms of the interface force, F_{PWAS}, and the axial and flexural dynamics of the plate. Discarding the time dependence, we write:

$$\hat{u}_{\text{PWAS}}(\omega) = \frac{\hat{F}_{\text{PWAS}}(\omega)}{a^2 \cdot \rho} \times \left[\frac{2}{h} \cdot \sum_k \frac{\left[r_a R_k(r_a) - \int_0^a R_k(r) H(r_a - r) dr\right] R_k(r_a)}{\left(\omega_k^2 - 2i\varsigma_k \omega\omega_k + \omega^2\right)} + \frac{h}{2} \cdot \sum_m \frac{\left[3Y_m(r_a) + r_a \cdot Y_m^{/}(r_a)\right] \cdot Y_m^{/}(r_a)}{\left(\omega_m^2 - 2i\varsigma_m \omega\omega_m + \omega^2\right)}\right] \tag{21}$$

Recalling Equation (1), we write $k_{\text{str}}(\omega) = \hat{} F_{\text{PWAS}}(\omega)/\hat{u}_{\text{PWAS}}(\omega)$, i.e.,

$$k_{\text{str}}(\omega) = a^2\rho \times \left[\frac{2}{h} \cdot \sum_k \frac{\left[r_a R_k(r_a) - \int_0^a R_k(r) H(r_a - r) dr\right] R_k(r_a)}{\left(\omega_k^2 - 2i\varsigma_k \omega\omega_k + \omega^2\right)} + \frac{h}{2} \cdot \sum_m \frac{\left[3Y_m(r_a) + r_a \cdot Y_m^{/}(r_a)\right] \cdot Y_m^{/}(r_a)}{\left(\omega_m^2 - 2i\varsigma_m \omega\omega_m + \omega^2\right)}\right]^{-1} \tag{22}$$

Upon inversion, we can also obtain the frequency response function (FRF) of the structure when subjected to PWAS excitation:

$$\text{FRF}_{\text{str}}(\omega) = \frac{1}{a^2\rho} \times \left[\frac{2}{h} \cdot \sum_k \frac{\left[r_a R_k(r_a) - \int_0^a R_k(r) H(r_a - r) dr\right] R_k(r_a)}{\left(\omega_k^2 - 2i\varsigma_k \omega\omega_k + \omega^2\right)} + \frac{h}{2} \cdot \sum_m \frac{\left[3Y_m(r_a) + r_a \cdot Y_m^{/}(r_a)\right] \cdot Y_m^{/}(r_a)}{\left(\omega_m^2 - 2i\varsigma_m \omega\omega_m + \omega^2\right)}\right] \tag{23}$$

3 Model Validation Through Numerical and Experimental Results

A series of experiments were conducted on thin-gage aluminum plates to validate the theoretical results. The set of specimens consisted of five identical circular plates manufactured from 2024 aluminum. The diameter of each plate was 100 mm and the thickness was 0.8 mm. Each plate was instrumented at its center with a 7 mm diameter piezoelectric wafer active sensor (PWAS). During the experiments, the specimens were supported on packing foam to simulate free boundary conditions. Impedance data was taken using a HP 4194A Impedance Analyzer. The spectra

collected on the five specimens showed very little variation from specimen to specimen (1% standard deviation in the resonance frequencies as identified from the E/M impedance real part spectra Re(Z)).

To validate the theory, we compared the experimental Re(Z) spectrum with the theoretical Re(Z) and the theoretical FRF spectrum. The FRF spectrum was utilized to illustrate the fact that the Re(Z) spectrum reflects the structural dynamics, i.e., the peaks of the Re(Z) spectrum coincide with the peaks the FRF peaks, which are the structural resonances. Figure 3(a) shows the FRF spectrum calculated with Equation (23), using $r_a = 3.5\,\text{mm}$, $a = 50\,\text{mm}$, $h = 0.8\,\text{mm}$, $\zeta_k = 0.07\%$, and $\zeta_m = 0.4\%$. The frequency range was 0.5–40 kHz. Six flexural resonances and one axial resonance were captured. The numerical values are given in Table 1. The match between the theoretical and experimental resonance values was very good. For most modes, the matching error is less than 1%. Two exceptions are noted: (i) the first flexural frequency has a matching error of −7.7%. This can be attributed to experimental error, since the E/M impedance does not work as well at low frequencies as it works at high frequencies, and hence the peak of the first flexural mode is very weak. (ii) The first axial mode has 2% error, which can be attributed to slight imperfections in the plate contour.

Figure 3(b) compares the experimental and theoretical Re(Z). The theoretical Re(Z) was calculated with a modification of Equation (10). The modifications consisted in introducing a multiplicative correction factor a/r_a, in front of the stiffness ratio $\chi(\omega)$. This correction factor was needed to account for difference between the k_{str} distributed over the radius of the plate and the k_{PZT} distributed over the radius of the sensor. The modified formula was:

$$Z(\omega) = \left\{ i\omega C\left(1 - k_p^2\right) \cdot \left[1 + \frac{k_p^2}{1 - k_p^2} \frac{(1 + \nu_a) J_1(\varphi_a)}{\varphi_a J_0(\varphi_a) - (1 - \nu_a) J_1(\varphi_a) - (a/r_a)\chi(\omega)(1 + \nu_a) J_1(\varphi_a)} \right] \right\}^{-1} \tag{24}$$

As seen in Figure 3(b), good matching between theoretical and experimental Re(Z) spectra was obtained. Thus, we can conclude that Equation (24) permits direct comparison of experimental and theoretical E/M impedance data, which is the aim of our analysis.

Although the simulation gives a good matching with experimental results, the theoretical model presented here is limited to the analysis of purely axis-symmetrical modes. In principle, the axis-symmetric assumption is consistent with the problem geometry in which a piezoelectric wafer active sensor, of circular geometry, is placed exactly at the center of a circular plate. However, if the sensor is slightly misaligned, non axis-symmetric modes will also be excited and will appear in the spectrum. This effect is observable in Figure 3, where the low-amplitude peaks that appear at 15, 24, and 33 kHz on the experimental curves have no match on the theoretical curves. These small peaks are due to non axis-symmetric modes that get parasitically excited due to slight misalignment in the placement of the sensor at the center of the plate.

4 Damage Detection in Circular Plates

Systematic experiments were performed on circular plates to assess the crack detection capabilities of the method. As shown schematically in Figure 4, five damage groups were considered: one group consisted of pristine plates (Group 0) and four groups consisted of plates with simulated cracks placed at increasing distance from the plate edge (Group 1–4). Each group contained five nominally 'identical' specimens. Thus, the statistical spread within each group could also be assessed. In our study, a 10-mm circumferential slit was used to simulate an in-service crack. The simulated crack was placed at a decreasing distance from the plate edge. The radial positions 40, 25, 10, and 3 mm from the sensor were considered (Figure 4).

The experiments were conducted over three frequency bands: 10–40; 10–150, and 300–450 kHz. The data was processed by plotting the real part of the E/M impedance spectrum, and determining

a damage metric to quantify the difference between spectra. The data for the 10–40 kHz band are shown in Figure 4. As damage is introduced in the plate, resonant frequency shifts, peaks splitting, and the appearance of new resonances are noticed. As the damage becomes more severe, these changes become more profound. The most profound changes are noticed for Group 4. For the higher frequency bands, similar behavior was observed.

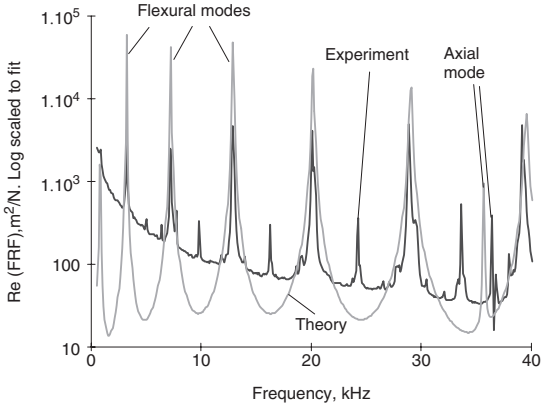

Figure 3 Experimental and calculated spectra for pristine plate specimen: (a) FRF in 0.5–40 kHz frequency range and (b) E/M impedance in 0.5–40 kHz frequency range.

4.1 Overall-Statistics Damage Metrics

The damage metric is a scalar quantity that results from the comparative processing of impedance spectra. The damage metric should reveal the difference between spectra due to damage presence. Ideally, the damage index would be a metric, which captures only the spectral features that are directly modified by the damage presence, while neglecting the variations due to normal operation conditions (i.e., statistical difference within a population of specimens, and expected changes in temperature, pressure, ambient vibrations, etc.). To date, several damage metrics have been used to compare impedance spectra and assess the presence of damage. Among them, the most popular are [6]: the root mean square deviation (RMSD), the mean absolute percentage deviation (MAPD), and the correlation coefficient deviation (CCD). The mathematical expressions for these metrics, given in terms of the impedance real part Re (Z), are as follows:

$$\mathrm{RMSD} = \sqrt{\sum_N \left[\mathrm{Re}(Z_i) - \mathrm{Re}(Z_i^0)\right]^2 / \sum_N \left[\mathrm{Re}(Z_i^0)\right]^2} \tag{25}$$

$$\mathrm{MAPD} = \sum_N \left|\left[\mathrm{Re}(Z_i) - \mathrm{Re}(Z_i^0)\right]/\mathrm{Re}(Z_i^0)\right|, \tag{26}$$

$$\mathrm{CCD} = 1 - \mathrm{CC}, \text{where,}$$

$$\mathrm{CC} = \frac{1}{\sigma_Z \sigma_{Z^0}} \sum_N \left[\mathrm{Re}(Z_i) - \mathrm{Re}(\bar{Z})\right] \times \left[\mathrm{Re}(Z_i^0) - \mathrm{Re}(\bar{Z}^0)\right], \tag{27}$$

where, N is the number of frequencies in the spectrum and the superscript 0 signifies the pristine state of the structure. The symbols $\bar{Z}$, $\bar{Z}^0$

Table 1 Theoretical and experimental results for a circular plate with a sensor installed in the center.

Frequency #	*1*	*2*	*3*	*4*	*5*	*6*	*7*	*8*
Mode	F	F	F	F	F	F	A	F
Calc. (kHz)	0.742	3.152	7.188	12.841	20.111	29.997	35.629	39.498
Exp. (kHz)	0.799	3.168	7.182	12.844	20.053	28.844	36.348	39.115
Error, Δ%	−7.708	−0.520	0.078	−0.023	0.288	0.528	1.978	0.97

Legend: F = flexural mode; A = axial mode.

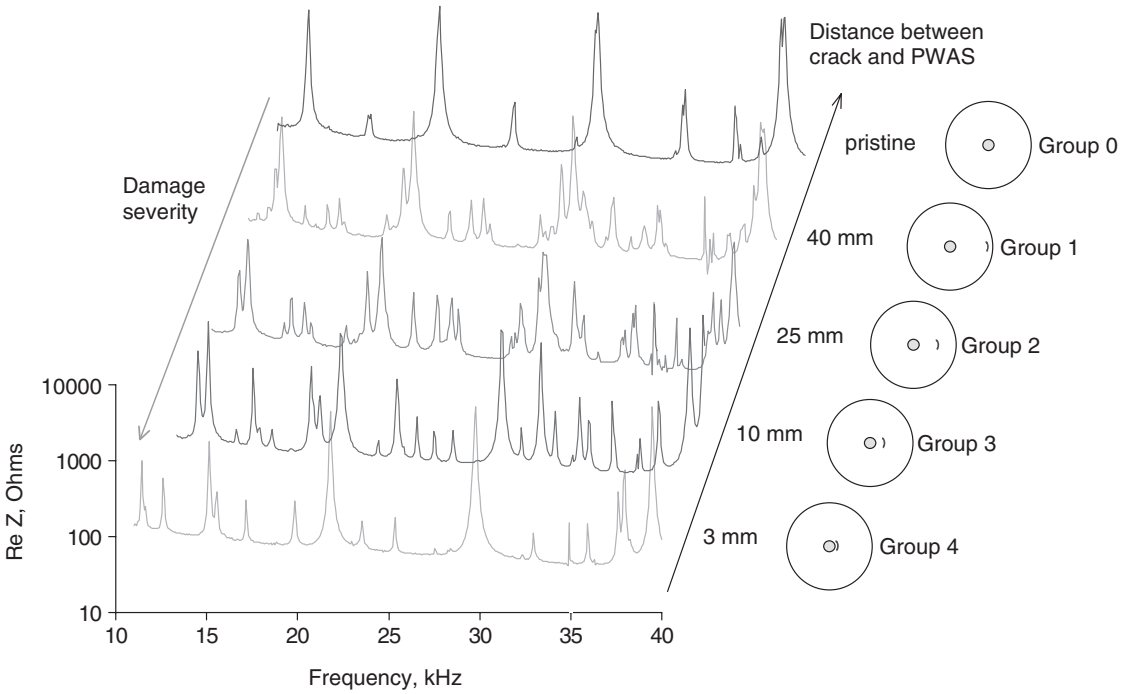

Figure 4 Dependence of the E/M impedance spectra on the location of damage.

signify mean values, while σ_Z, σ_{Z^0} signify standard deviations.

Equations (25)–(27) yield a scalar number, which represent the relationship between the compared spectra. Thus, we expect that the resonant frequency shifts, the peaks splitting, and the appearance of new resonances that appear in the spectrum will alter the damage index and thus, signal the presence of damage. The advantage of using Equations (25)–(27) is that the impedance spectrum does not need any preprocessing, i.e., the data obtained from the measurement equipment can be directly used to calculate the damage index. In our experimental study, we used the scalar values of RMSD, MAPD, and CCD calculated with Equations (25)–(27) to classify the different groups of specimens presented in Figure 4.

The data processing results for the three frequency bands (10–40, 10–150, 300–450 kHz) are summarized in Table 2. It seems that the CCD metric is more sensitive to the damage presence than RMSD and MAPD. However, it was also observed that for the 10–40 kHz and 10–150 kHz frequency bands, the CCD variation with damage severity is not monotonic. This indicates that the choice of the frequency band may play a significant role in the classification process: the frequency band with highest density of peaks is recommended. Hence, we used the frequency band 300–450 kHz for further data analysis. Figure 5 presents the variation of the metric CCD^7 with the crack distance from the plate center. It is apparent that as the crack is placed further away, and its influence diminishes, the value of the CCD^7 metric also diminishes. In fact, the CCD^7 damage metric tends to linearly decrease with the crack position, which may be very useful in automated damage assessment.

4.2 Probabilistic Neural Networks (PNN) for Damage Identification

Probabilistic neural networks (PNN) were first proposed by Specht [21] as an efficient tool for solving classification problems. In contrast to other neural network algorithms used for damage identification [22], PNN has statistically derived activation function and utilizes Bayesian decision strategy for the classification problem. The kernel-based approach to probability density function (PDF) approximation is used. This

Table 2 Overall-statistics damage metrics for various frequency bands.

Frequency band	*11–40* kHz				*11–150* kHz				*300–450* kHz			
compared groups (%)	*0–1*	*0–2*	*0–3*	*0–4*	*0–1*	*0–2*	*0–3*	*0–4*	*0–1*	*0–2*	*0–3*	*0–4*
RMSD	122	116	94	108	144	161	109	118	93	96	102	107
MAPD	107	89	102	180	241	259	170	183	189	115	142	242
CCD	84	75	53	100	93	91	52	96	81	85	87	89

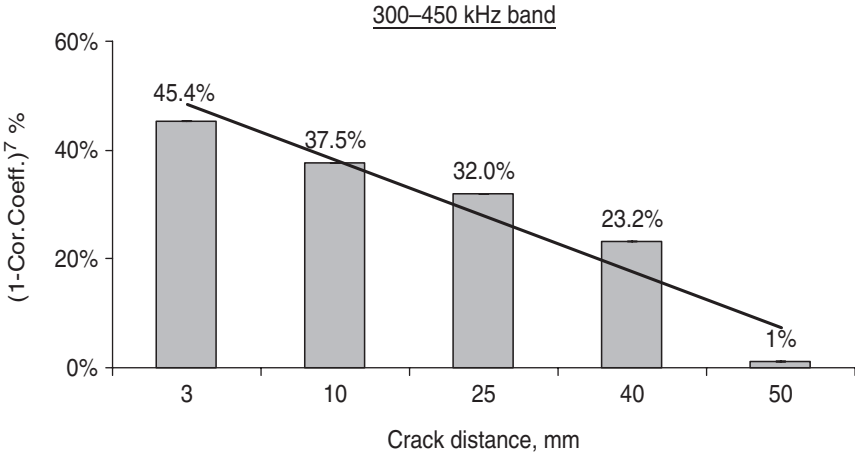

Figure 5 Monotonic variation of the CCD^7 damage metric with the crack radial position on a 50-mm radius plate in the 300–450 kHz band.

method, introduced by Parzen [23], permits the construction of the PDF of any sample of data without any a priori probabilistic hypothesis [24]. The PDF reconstruction is achieved by approximating each sample point with kernel function(s) to obtain a smooth continuous approximation of the probability distribution [25]. In other words, using kernel technique, it is possible to map a pattern space (data sample) into the feature space (classes). However, the result of such transformation should retain essential information presented in the data sample and be free of redundant information, which may contaminate the feature space. In this study, we used the resonance frequencies as a data sample to classify spectra according to the damage severity. The classical multivariate Gaussian kernel was chosen for PNN implementation. In the original Specht's formulation [21], this kernel was expressed as:

$$p_A(x) = \frac{1}{n \cdot (2\pi)^{d/2} \sigma^d} \sum_{i=1}^{n} \exp\left(-\frac{(x - x_{Ai})^T (x - x_{Ai})}{2\sigma^2} \right) \tag{28}$$

where i is a pattern number, x_{Ai} is the ith training pattern from A category, n is total number of training patterns, d is dimensionality of measurement space, and σ is a spread parameter. Although the Gaussian kernel function was used in this work, its form is generally not limited to being Gaussian. Burrascano et al. [26] used a PNN with different kernel types for damage identification.

4.3 Damage Detection in Circular Plates with Probabilistic Neural Networks

To construct the PNN input vectors, the spectra of Figure 4 were processed to extract the resonance frequencies for each class. At the beginning, a small number of frequencies was used, namely the four dominant frequencies that appear in the pristine plate. In this case, the PNN consisted of four inputs, five neurons in the pattern layer, and five neurons in the output layer. The number of inputs corresponds to number of resonance frequencies. The pattern layer is formed

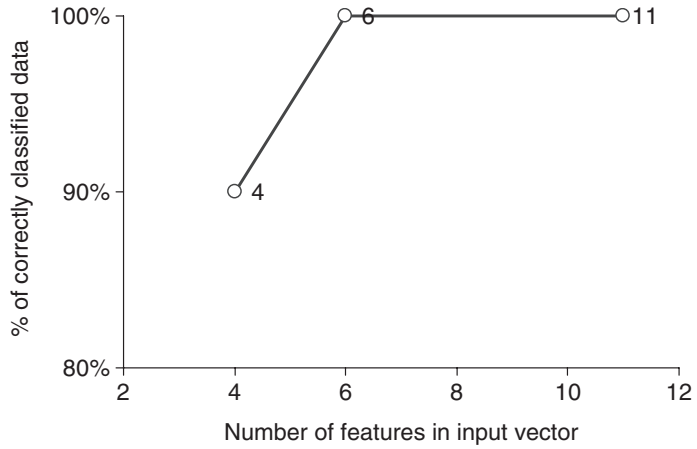

Figure 6 Number of features in input vector of PNN vs percent of correctly classified data.

according to numbers of input/target pairs. The number of output neurons represents the categories in which the input data is supposed to be classified. For training, we initially used one vector from each class. Then, the other four vectors from each class (a total of 20) were used for validation. The PNN was able to successfully classify the high and intermediate damage levels (Groups 2, 3, 4). However, for weak damage (Group 1), the PNN produces inconsistent results. To correct this, we tried to increase the number of training vectors in Groups 1 and 0. The incidence of misclassification diminished, but it did not disappear completely. Even when the maximum number of training vectors was considered, some misclassification between Groups 0 and 1 still occurred.

To solve the misclassification problem at weak damage levels, we increased the size of the input vectors. This was achieved by considering not only the four dominant frequencies, but also the two secondary frequencies that appear in the pristine spectrum. Thus, the size of the input vector became six. Then, we choose one input vector from each group for training. The remaining four vectors in each group (a total of 20 in the data set) were used for validation. This time, the classification was perfect. Due to the additional information, the PNN was able to distinguish even the most difficult classification cases, i.e., the weak damage class (Group 1). Furthermore, regardless of the choice of the training vector, all the validation data were correctly classified into five classes.

Further in our study, we considered an extension of the features vector size by incorporating the new resonances that appeared in the damaged plates but were not present in the pristine plates. This feature plays an important role in distinguishing healthy structures from damaged structures, especially when the damage is incipient or located away from the sensor. To achieve this, we expanded the features vector to incorporate the new resonance that appeared in the damaged plates. In order to preserve dimensionality, the pristine plates vectors were zero filled as needed. Thus, the features vector size was expanded to eleven. Then, one vector from each group was used for training, and the rest for validation. The PNN was again able to correctly classify data regardless of the choice of the training vectors. Figure 6 presents the percent of correct classified data versus number of features in the input vectors of PNN. The good classification results obtained with PNN encouraged us to further use this method for damage classification in aircraft structural specimens.

5 Damage Identification in Aging Aircraft Panels

Realistic specimens representative of real-life aerospace structures with aging-induced damage

(cracks and corrosion) were developed at Sandia National Laboratories and sent to us for testing. These specimens are aircraft panels with structural details typical of metallic aircraft structures (rivets, splices, stiffeners, etc.) Their presence complicates the structural dynamics and makes the damage detection task more difficult. The specimens were made of 1 mm (0.040″) thick 2024-T3 Al-clad sheet assembled with 4.2 mm (0.166″) diameter countersunk rivets. Cracks were simulated with Electric Discharge Machine (EDM). In our study, we investigated crack damage and considered two specimens: pristine (Panel 0), and damaged (Panel 1). The objective of the experiment was to detect a 12.7 mm (0.5″) simulated crack originating from a rivet hole (Figure 7). The panels were instrumented with eight sensors, four on each panel (Table 3). On each panel, two sensors were placed in the medium field (100 mm from the crack location), and two in the near field (10 mm from the crack location). It was anticipated that sensors placed in a similar configuration with respect to structural details (rivets, stiffeners, etc.) would give similar E/M impedance spectra. It was also anticipated that the presence of damage would change the sensors readings. Referring to Figure 7, we observe that the sensors S1, S2, S3, S5, S6, and S7 are in pristine regions, and should give similar readings, while S4 and S8 are in damaged regions, and should give different readings. High frequency E/M impedance spectrum was collected for each sensor in the 200–550 kHz band, which shows a high density of resonance peaks. During the experiment, both aircraft panels were supported on foam to simulate free boundary conditions. The data was collected with HP 4194A impedance analyzer and through GPIB interface loaded into PC for further processing.

5.1 Classification of Crack Damage in the PWAS Near-field

The near-field PWAS were S5, S6, S7, and S8. All were placed in similar structural configurations. Hence, in the absence of damage, all should give similar impedance spectra. However, S8 is close to the simulated crack originating from the rivet hole. Hence, it was anticipated that S8 should give an impedance spectrum different from that of S5, S6, and S7. The change in the spectrum would be due to the presence of crack damage. Hence, we call S5, S6, and S7 'pristine,' and S8 'damage.' Figure 8(a) shows the superposition of the spectra obtained from these sensors. Examination of these spectra reveals that sensor S8, placed next to the crack, has two distinct features that make it different from the other three spectra: (a) a higher density of peaks; (b) an elevated dereverberated response in the 400–450 kHz range. On the other hand, the spectra of sensors S5, S6, and S7 do not show significant differences. To quantify these results, we used two methods: (i) overall statistics metrics of the dereverberated response (DR), and (ii) probabilistic neural networks (PNN).

Figure 8(b) shows the DR curves extracted from the Figure 8(a) spectra using 9th order polynomial fit. It is clear that three DRs for 'pristine' scenario (S5, S6, and S7) are very similar. In contrast, the DR for the 'damage' scenario, S8, is clearly different. To quantify these DR differences, we used the overall-statistics damage metrics defined by Equations (25)–(27), i.e., RMSD, MAPD, and CCD. The results of this analysis are presented in Table 4. Two sets of results are presented: (a) Pristine versus Pristine, and (b) Damage versus Pristine. The former is used to quantify the statistical differences between members of the same class, i.e., the 'pristine' sensors S5, S6, and S7. The latter is used to quantify the differences the 'damage' sensor S8, and any of the 'pristine' sensors, S5, S6, S7. Then, in each set, the mean value was calculated. Examination of Table 4 indicates that the RMSD and MAPD values for the 'damage' case are almost double that for the 'pristine' case. This indicates good damage detection capability. However, the CCD values indicate an even better detection capability, since the value for the 'damage' case is an order of magnitude larger than that for the 'pristine' case (6.64% vs. 0.55%). This confirms that CCD is potentially a very powerful damage detection metric. The mean CCD, MAPD, RMSD values are presented graphically in Figure 9. The stronger detection capability of CCD metric is again highlighted.

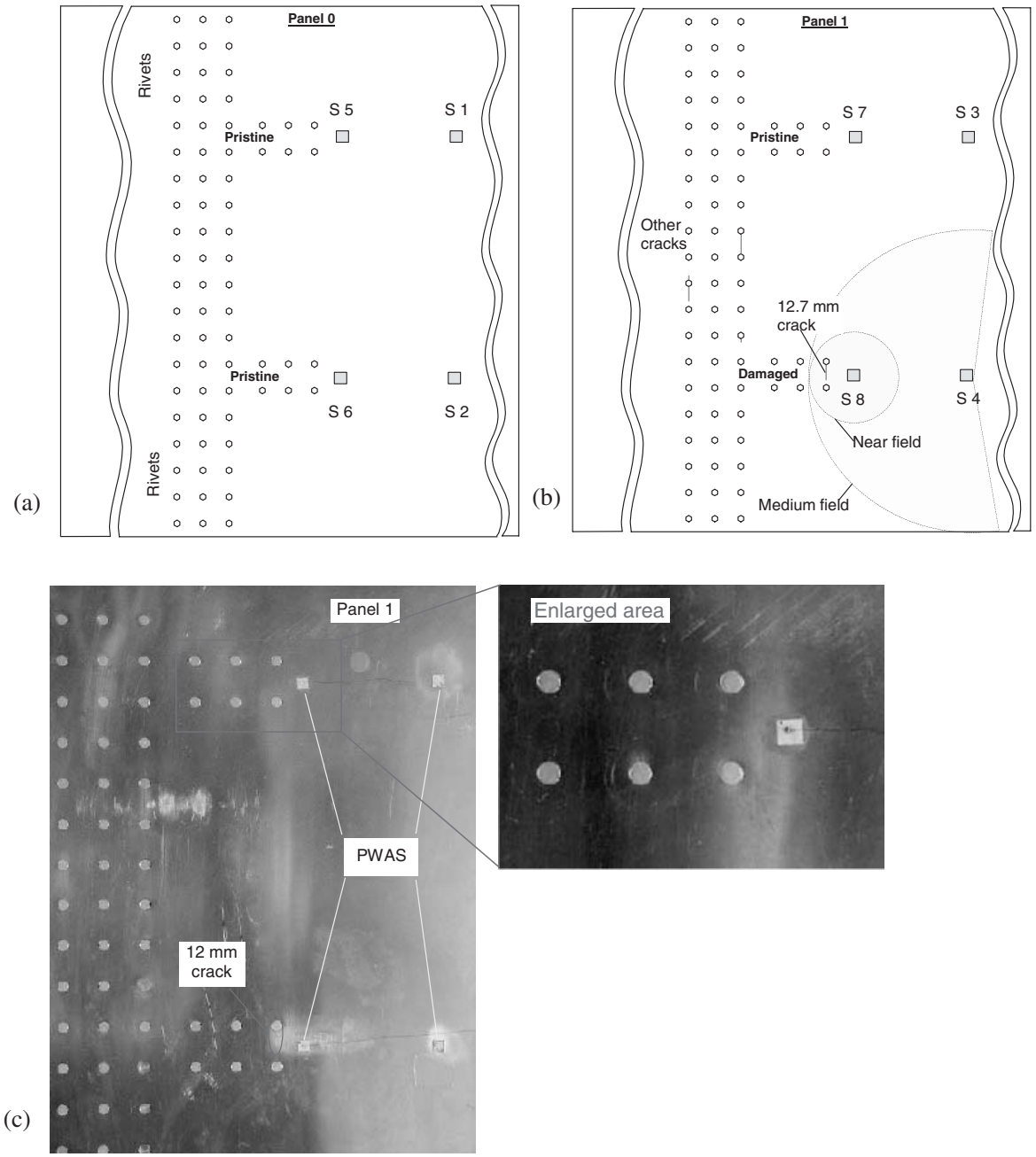

Figure 7 Schematics of the aging aircraft panel specimens and PWAS configuration: (a) panel 0, sensors S1, S2, S5, S6; (b) panel 1, sensors S3, S4, S7, S8 and (c) aircraft skin panel 1 with enlarged area of PWAS installation.

Table 3 Position of PWAS on aircraft panels.

	Panel 0		*Panel 1*	
	Pristine	*Pristine*	*Pristine*	*Crack*
Medium field	S1	S2	S3	S4
Near field	S5	S6	S7	S8

5.2 Classification of Crack Damage in the PWAS Medium Field

The medium field experiment was designed to estimate the ability of PWAS to detect damage in a wider area. In this study, the medium field is

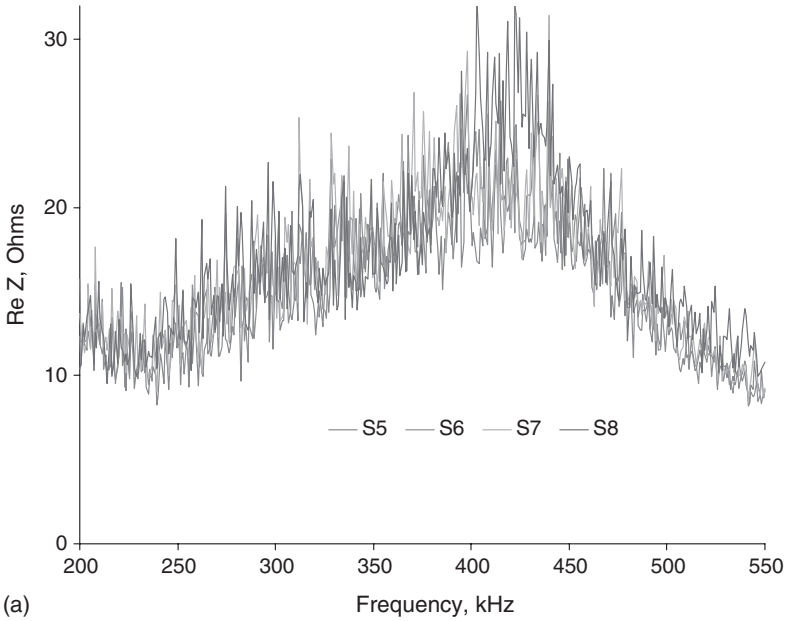

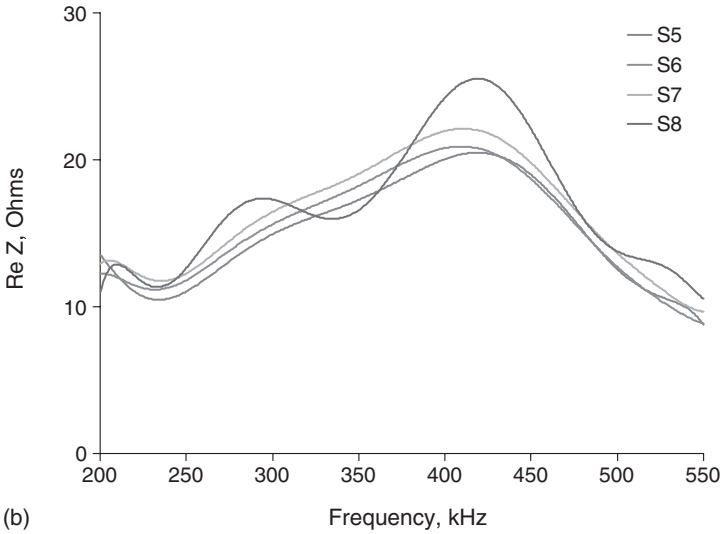

Figure 8 (a) Superposition of PWAS near field E/M impedance spectra in the 200–550 kHz band and (b) dereverberated response.

Table 4 Response of RMSD, MAPD, and CCD metrics to near field damage (S5, S6, S7 = pristine, S8 = damage).

Class	*Pristine vs. Pristine* (%)			*Damage vs. Pristine* (%)		
Sensors	*S5–S6*	*S5–S7*	*S6–S7*	*S5–S8*	*S6–S8*	*S7–S8*
RMSD	4.09	8.74 6.18	5.71	15.64 13.28	14.10	10.10
MAPD	3.75	8.43 6.02	5.88	13.26	11.89 11.07	8.05
CCD	0.94	0.63 0.55	0.07	5.70	7.45 6.64	6.77

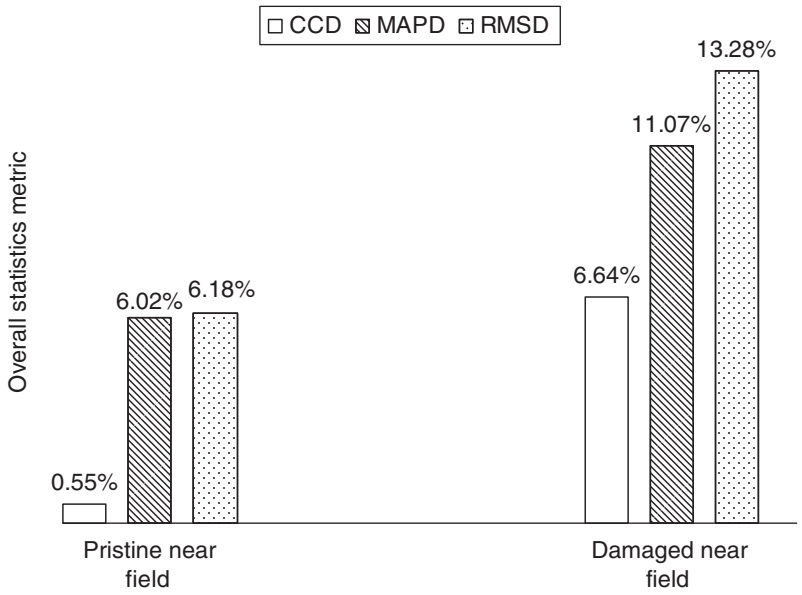

Figure 9 Overall-statistics damage metrics for comparison as calculated on the near field spectra.

called the area with a radius of about 100 mm where the detection of damage is still possible, but the effect of damage did not manifest as drastically on the E/M impedance spectra as in the near field. The distance between PWAS and crack for the medium field experiment was eight times bigger than that for near field experiment. The relative size of near field and medium field of PWAS is depicted in Figure 7(b).

The medium field PWAS were S1, S2, S3, and S4. They were located approximately 100 mm from the first rivets in the horizontal rows of rivets. Though placed at different locations, all four PWAS were placed in similar structural situations. Hence, in the absence of damage, they should give the same spectral readings. However, S4 is not exactly in the same situation, due to the presence of the 12.7 mm simulated crack originating from the first rivet hole (Figure 7). Therefore, the S4 spectrum is expected to be slightly different. Since S4 is not in the crack near field, this difference is not expected to be as large as that observed on S8 in the near-field experiments. To summarize, S1, S2, and S3 are in 'pristine' situations, while S4 is in 'damage' situation.

The E/M impedance spectra for S1, S2, S3, and S4 are presented in Figure 10. It could be noted that the spectrum of the 'damage' sensor S4 displays some higher amplitudes of some of the spectral resonances in comparison with the spectra for S1, S2, and S3. On the other hand, no significant difference was observed between the S1, S2, and S3 spectra, which are in the 'pristine' class. However, the change due to damage are much slighter than those observed in the near-field experiment, and no change in the dereverberated response could be observed. In other words, the dereverberated responses observed in the 'pristine' (S1, S2, and S3) and 'damaged' (S4) classes follow similar general patterns. For this reason, the analysis of the dereverberated response did not yield practical results.

To compare the medium-field spectra, we used the PNN algorithm. As in the case of the circular plates, the spectral feature considered in the analysis were the resonance frequencies. A feature extraction algorithm was used to obtain the feature vectors. The algorithm was based on a search window and amplitude thresholds. The 48 extracted features are shown graphically in Figure 11. Figure 11(a) shows the S1 results corresponding to a 'pristine' scenario, while Figure 11(b) shows the S4 results corresponding to a 'damage' scenario. The resonance peaks picked by the feature extraction algorithm are marked with a cross in the data point. It can

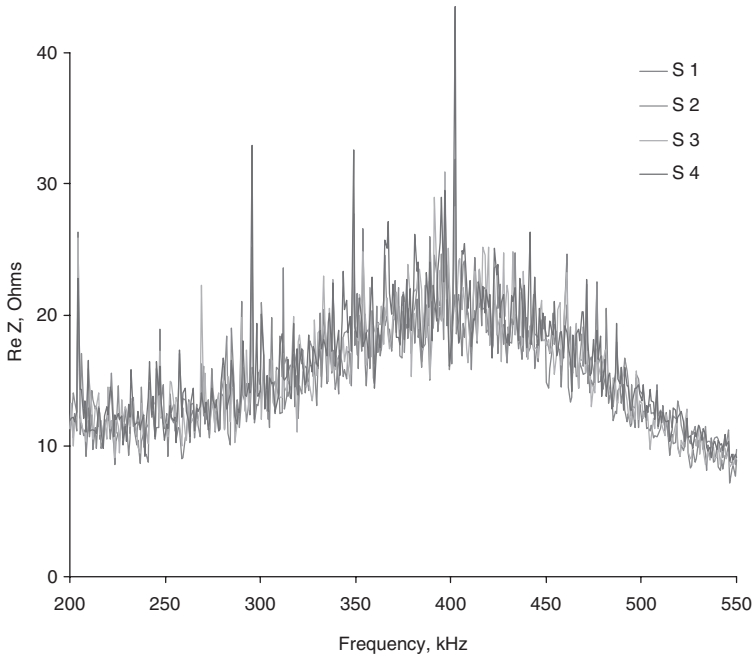

Figure 10 Superposition of PWAS medium field E/M impedance spectra in the 200–550 kHz band.

be seen that the resonance frequencies for the 'pristine' and 'damaged' scenarios are different. For example, the 'pristine' scenario features several peaks above 500 kHz, while the 'damage' scenario does not show any peaks in this bandwidth. As a result of this process, we were able to construct four feature vectors, each 48 long, that served as inputs to the PNN. Of these, three vectors represented 'pristine' condition (S1, S2, and S3) while the fourth vector represented a 'damage' condition (S4).

The PNN was designed to classify data into two classes: 'pristine' and 'damage.' Since we have three 'pristine' input vectors and one 'damaged' input vector, we decided to use one of the three 'pristine' input vectors for training, and the other three vectors (two 'pristine' and one 'damage') for validation. (No training was feasible for 'damaged' scenario). This created a dichotomous situation, in which the PNN would recognize data when it belongs to the 'pristine' class, and would reject it when it did not belong to the 'pristine' class. Thus, the 'damaged' situation was recognized as 'nonpristine'. We would like to emphasize that this type of classification problem often occurs in practice where response of structure in pristine condition is usually known and response in damaged condition is frequently unknown. The results of the PNN study indicated that, regardless of choice of training vector for the 'pristine' class, the PNN was able to correctly classify data into the correspondent classes. This is indicated in Table 5, where T indicates training, and V validation.

After successfully using the PNN method to detect damage in the medium field, we backtracked and used it for damage classification in the near field. The raw spectra obtained for the near field were processed with the features extraction algorithm using the same settings as for the medium field experiment. The PNN design, training, and validation were similar to the medium field. The PNN correctly classified data into 'pristine' and 'damaged' for all training vector choices. We conclude that the classification problem for both medium field and near field problems on aging aircraft panels can be successfully solved with the PNN algorithm.

Also noticed in our investigation was the localization property of the E/M impedance method. As seen in Figure 7, Panel 1 had also other simulated cracks. However, these cracks

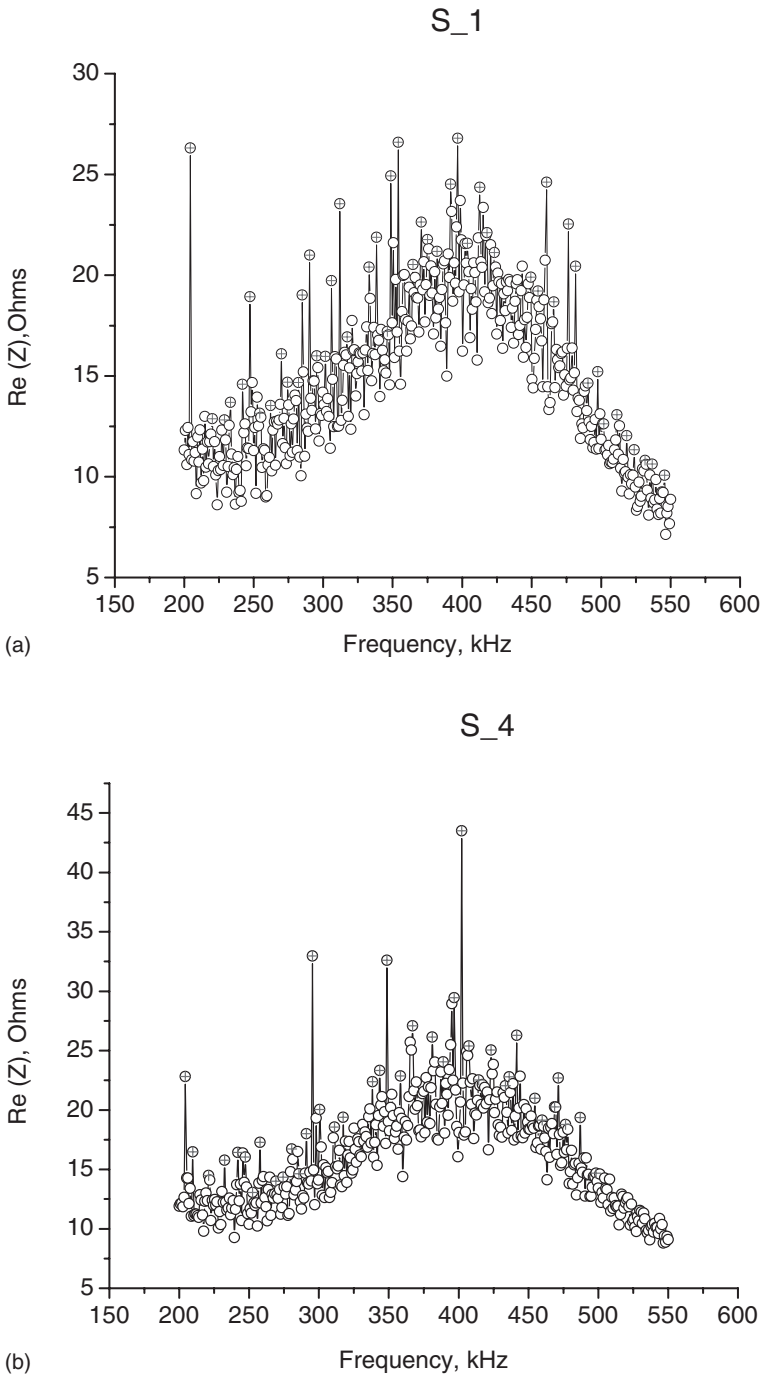

Figure 11 E/M impedance spectra for damage detection experiment in the PWAS medium field: (a) sensor S1 – 'pristine' case and (b) sensor S4 – 'damaged' case.

were away from the sensors, and hence outside the sensors sensing range. For this reason, these cracks did not noticeably influence the sensors readings. The localization property of the E/M impedance method is important for finding the approximate location of the damage on the structure. Since the E/M impedance method is intended for structural health monitoring,

Table 5 Damage identification in aircraft panels using probabilistic neural network classification.

	Medium field				*Near field*				
Vector	*S1*	*S2*	*S3*	*S4*	*S5*	*S6*	*S7*	*S8*	
Test									
I	T	V	V	V	T	V	V	V	in
	–	0	0	**1**	–	0	0	**1**	out
II	V	T	V	V	V	T	V	V	in
	0	–	0	**1**	0	–	0	**1**	out
III	V	V	T	V	V	V	T	V	in
	0	0	–	**1**	0	0	–	**1**	out

an approximate location of the damage would be sufficient for a first alert. Further investigation of the exact damage location and its severity would make the object of detailed NDE investigation, once the vehicle has been pulled out of service due to structural health deficiency.

6 Summary and Conclusions

The theoretical and practical aspects of the application of E/M impedance method to the structural health monitoring (SHM) of thin-wall structures using piezoelectric wafer active sensors (PWAS) was discussed. A circular plate model, which accounts for sensor structure interaction in 2-D geometry, was derived and validated through experimental testing. The model considers both the structural dynamics and the sensor dynamics. In the structural dynamics, both the axial and the flexural vibrations were considered. The structural dynamics was incorporated into the model through the pointwise dynamic stiffness presented by the structure to the PWAS. The analytical model predicts the electro-mechanical (E/M) impedance response, as it would be measured at the PWAS terminals. The real part of the E/M impedance reflects with fidelity the natural frequencies of the structure on which the PWAS is mounted. Through experimental tests, we were able to validate both the model capability to correctly predict the E/M impedance, and the determination of the structural frequencies from the E/M impedance real part. Thus, it was verified that PWAS, in conjunction with the E/M impedance, act as self-excited high-frequency modal sensors that correctly sense the structural dynamics.

Damage detection experiments were performed on circular plates and on aircraft panels. It was observed that the presence of damage (through the thickness cracks modeled with 10 mm and 12.7 mm slits) significantly modifies the E/M impedance spectrum, which features frequency shifts, peaks splitting, and appearance of new harmonics. The rate of changes in the spectrum increases with the severity of damage. To quantify these changes and classify the spectra according to the severity of damage, two approaches were used: (a) overall-statistics damage metrics; and (b) probabilistic neural networks (PNN). In the overall-statistics damage metrics approach, root mean square deviation (RMSD), mean absolute percentage deviation (MAPD), and correlation coefficient deviation (CCD) were considered. Through the circular plates experiments, it was found that CCD[7] damage metric is a satisfactory classifier in the high frequency band where the resonance peaks density is high (300–450 kHz). In the PNN approach, the spectral data was first preprocessed with a features extraction algorithm that generated the features vectors that serve as input vectors to the PNN. In our investigation, we used features consisting of the numerical values of the resonance frequencies. A reduced-size features vector, containing only the four dominant resonance frequencies, permitted the PNN to classify correctly the medium and severe damage scenarios. However, the weak damage scenario gave some misclassifications. This problem was overcome by increasing the input vector size to six resonance frequencies. Further, we studied the adaptive resizing of the input vector such

as to accommodate the new frequencies that appeared in the spectrum when damage was present. Again, all the damage cases were properly classified.

Aging aircraft panels were used to study the ability of the E/M impedance method to capture incipient damage represented by a crack growing from a rivet hole. The experiments were conducted with four PWAS placed in the near field and other four placed in the medium field. Data was collected in the 200–550 kHz band. The overall statistics damage metrics could only be used for the near-field case, when the 'damage' spectrum showed a clear change in the dereverberated response. In this case, the CDD metric, applied to the dereverberated response, showed the biggest change between the 'pristine' and the 'damaged' situations. The PNN approach was able to correctly classify both near-field and medium-field spectra. The PNN inputs consisted of 48 long features vectors extracted from the spectrum with a peak-selection algorithm. The PNN had to select between four spectra, of which only one was pristine. The procedure was to train the PNN on one of the 'pristine' scenarios, and then present the remainder three for validation. In all cases, correct classification was obtained, and the 'damage' scenario was recognized as 'non-pristine.' We conclude that PNN, with the appropriate choice of the spread constant, shows good potential for attacking and solving the complex real-life classification problems associated with high-frequency spectrum-based damage detection.

The example of SHM of aging aircraft specimens shows that permanently attached unobtrusive and minimally invasive PWAS, used in conjunction with E/M impedance method, can be successfully used to assess the presence of incipient damage through E/M impedance spectra classification. The E/M impedance method and the wave propagation method form complementary techniques and enabling technologies for *in-situ* structural health monitoring [27,28].

Acknowledgments

This work was partially supported by the Department of Energy through the Sandia National Laboratories, contract doc. #BF0133; National Science Foundation awards CMS-9908293 and INT-9904493, and USAF/NRC SFFP at AFRL/MLLP, WPAFB.

References

1. Chaudhry, Z., Joseph, T., Sun, F. and Rogers, C. (1995). Local-area health monitoring of aircraft via piezoelectric actuator/sensor patches. In: *Proceedings*, *SPIE North American Conference on Smart Structures and Materials*, San Diego, CA, 26 Feb–3 March, Vol. 2443, pp. 268–276.
2. Giurgiutiu, V. and Zagrai, A.N. (2000). Damage detection in simulated aging-aircraft panels using the electro-mechanical impedance technique. In: *Proceedings of Adaptive Structure and Material Systems Symposium*, ASME Winter Annual Meeting, Orlando, FL, 5–10 Nov.
3. Raju, V., Park, G. and Cudney, H.H. (1998). Impedance based health monitoring of composite reinforced structures. In: *Proceedings of the 9th International Conference on Adaptive Structures and Technologies*, Cambridge, MA, 14–16 October.
4. Giurgiutiu, V. and Rogers, C.A. (1999). Recent progress in the application of E/M impedance method to structural health monitoring, damage detection and failure prevention. In: *2nd International Workshop of Structural Health Monitoring*, Stanford U., CA, 8–10 Sept pp. 298–307.
5. Park, G. and Inman, D.J. (2001). Impedance-based structural health monitoring, monograph: In: Woo, S.C. (ed), *Nondestructive Testing and Evaluation Methods for Infrastructure Condition Assessment*, New York, NY: Kluwer Academic Publishers.
6. Tseng, K.K.-H., Soh, C.K., and Naidu, A.S.K. (June 2001). Non-parametric damage detection and characterization using smart piezoceramic material, *Smart Material and Structures 11*(3), 317–329.
7. Liang, C., Sun, F.P. and Rogers C.A. (January 1994). Coupled electro-mechanical analysis of adaptive material system-determination of the actuator power consumption and system energy transfer, *Journal of Intelligent Material Systems and Structures*, *5*, 12–20.
8. Sun, F.P., Liang, C. and Rogers, C.A. (1994). Experimental modal testing using piezoceramic patches as collocated sensors-actuators. In: *Proceeding of the 1994 SEM Spring Conference & Exhibits*, Baltimore, MI, 6–8 June, 1994
9. Zhou, S.W., Liang, C. and Rogers, C.A. (1996). An impedance-based system modeling approach for induced strain actuator-driven structures. *Journal of Vibration and Acoustics*, *118*(3), 323–331.

10. Esteban, J. (July 1996). Analysis of the sensing region of a PZT actuator-sensor, PhD Dissertation, Virginia Polytechnic Institute and State University.
11. Park, G., Cudney, H.H. and Inman, D.J. (2000). An integrated health monitoring technique using structural impedance sensors. *Journal of Intelligent Material Systems and Structures*, *11*(6), 448–455.
12. Giurgiutiu, V. and Zagrai, A.N. (January 2002). Embedded self-sensing piezoelectric active sensors for on-line structural identification, transactions of ASME. *Journal of Vibration and Acoustics*, *124*, 116–125
13. Onoe, Mario and Jumonji, Hiromichi (1967). Useful formulas for piezoelectric ceramic resonators and their application to measurement of parameters, IRE, Number 4, Part 2.
14. Pugachev, S.I., Ganopolsky, V.V., Kasatkin, B.A., Legysha F.F. and Prydko, N.I. (1984). Piezoceramic transducers, handbook, sudostroenie, St.- Petersburg, (in Russian).
15. IEEE Std. 176 (1987), *IEEE Standard on Piezoelectricity*, The Institute of Electrical and Electronics Engineers, Inc.
16. Liessa, A. (1969). Vibration of plates, Published for the Acoustical Society of America through the American Institute of Physics, Reprinted in 1993.
17. Soedel, W. (1993). Vibrations of plates and shells, Marcel Dekker, Inc.
18. Rao, J.S. (1999). Dynamics of plates. Marcel Dekker, Inc., Narosa Publishing House.
19. Itao, K. and Crandall, S.H. (1979). Natural modes and natural frequencies of uniform, circular, free-edge plates, *Journal of Applied Mechanics*, *46*, 448–453.
20. Zagrai, A.N. (May 2002). Piezoelectric-wafer active sensor electro-mechanical impedance structural health monitoring, PhD Dissertation, University of South Carolina.
21. Specht, D.F. (1990). Probabilistic neural networks, *Neural Networks*, *3*, 109–118.
22. Lopes, Jr.V., Park, G., Cudney, H. and Inman, D. (March 2000). Impedance based structural health monitoring with artificial neural network. *Journal of Intelligent Materials Systems and Structures*, *11*, 206–214.
23. Parzen, E. (1962). On Estimation of a probability density function and mode, *Annals of Mathematical Statistics*, *33*, 1065–1076.
24. Rasson, J.P. and Lissoir, S. (1998). Symbolic kernel discriminant analysis, NTTS '98, *International Seminar on New Techniques and Technologies for Statistics*.
25. Dunlea, S., Moriarty, P. and Fegan, D.J. (2001). Selection of TeV γ-rays using the kernel multivariate technique. In: *Proceedings of ICRC*.
26. Burrascano, P., Cardelli, E., Faba, A., Fiori, S. and Massinelli, A. (2001). Application of probabilistic neural networks to eddy current non destructive test problems, *EANN 2001 Conference*, Cagliari, Italy, 16–18 July.
27. Giurgiutiu, V., Zagrai, A.N. and Bao, J. (August 2002). Embedded active sensors for in-situ structural health monitoring of thin-wall structures, *ASME Journal of Pressure Vessel Technology*, *124*(3), 293–302.
28. Park, G., Sohn, H., Farrar, C.R. and Inman, D.J. (November 2003). Overview of piezoelectric impedance-based health monitoring and path forward, *Shock and Vibration Digest*, *35*(6), 451–463.